Chapter 5

Enhanced OER properties from nanocomposites of Co_3O_4 and MOF derived N/S/Zn-doped porous carbon

5.1. Introduction

The frequent exercise of non-renewable fuel sources in day-to-day life and industrial purposes gravely increases the greenhouse effect, and thus, switching from non-renewable to clean and renewable green energy is direly needed [168]. However, the bitter truth is that we are so dependent on non-renewable energy that immediate switching is impossible. Many governments worldwide are also trying to reduce dependence on non-renewable energy and encourage a gradual switch towards green energy. There are many approaches towards this switching like harvesting solar energy, wind energy, geothermal energy, hydroelectric power, O_2 and H_2 production through water-splitting, etc. However, solar energy harvesting is a costly process and creates much waste in the form of solar substrates. Wind energy setup is costly and a threat to wildlife and also creates low-level noise; the location-specific geothermal energy needs high initial cost and can cause earthquakes in extreme situations [189]. Hydroelectric power has the potential to supply a good amount of energy, but it needs to hold a large amount of water, and during the monsoon, sometimes floods happen in the nearby area to maintain those plants. The most promising, cheaper and favorable approach to producing clean and green energy is through water splitting [7].

The production of H_2 and O_2 at the cathode and anode through water splitting using nominal electrical energy is associated with hydrogen evolution reaction (HER) and oxygen evolution reaction (OER). The reaction at the cathode is supposed to be a fast process consisting of only two steps. While the reaction at the anode (OER) is identified as the kinetic barrier during the electrolysis of water, as it entails four steps reaction with simultaneous loss of electrons. The sluggish kinetics of OER ($4OH^- \rightarrow 2H_2O + O_2 + 4e^-$;

in basic medium and $2H_2O \rightarrow 4H^+ + O_2 + 4e^-$; in acid medium) require large reaction overpotentials both in acidic and basic media. Fundamentally, this limits the overall efficiency of the above process. At the same time, in the basic medium, OER is very slow due to the absorption of a large amount of OH^- ions in the active sites of the catalyst surface to form active OH^-. In the aqueous solution, this OH^- travels to the active end of the anodic surface and interacts with intermediate O* to form another intermediate OOH*, which changes to intermediate OO* after deprotonation. According to Gibbs's free energy theory ($\Delta G < 0$), a fixed potential difference causes as-released OO* to further react with OH^- in order to form O_2 [168]. Though RuO_2 or IrO_2 catalysts are regarded as ideal materials for catalytic activity towards OER, they suffer from a few noticeable drawbacks such as poor stability, inadequate reserves, high cost, and single functional catalytic activity [190]. Therefore, developing other durable and highly active OER catalysts with at least similar or outperforming catalytic activity is obligatory compared to RuO_2 or IrO_2, with high stability and low cost [191]. In this regard, the association of porous carbon-based and transition-metal-based materials [191, 82 and, 192] has attracted substantial research attention in the last few decades. Among the porous carbon-based nanomaterials, heteroatom doping has been a promising approach in catalytic activities toward energy storage and energy conversion applications [193]. Their better performance is due to the localization of charges near heteroatoms (commonly known as charge polarization) resulting from differences in electronegativity and spin density between heteroatoms and carbons [85]. Apart from this, such materials act as an excellent host that allows proper dispersion of metals, metal oxides, or other nanoparticles and enhances the conductivity of as-designed hybrid materials [85, 194]. On the other hand, transition metals supported on N-doped carbon catalysts usually exhibit satisfactory

oxygen reduction reaction (ORR) and OER performance due to high surface area facilitating enhanced active centres [195, 196]. Similarly, another dopant like S-atom containing p-orbitals in its outermost shell holds approximately similar electronegativity to carbon and can easily induce the polarization of neighbouring C and N atoms [197, 198]. Here, transition metals not only create metal node bridges with organic ligands but also act as Lewis's acid for other metal species (stabilizes the higher oxidation state of other metal oxides like oxides of cobalt, if any) but also direct the orientation of pores of carbon matrix which can promote the catalytic performance [199]. Thus, rendering N, S-dual-doping in the carbon matrix, an exceptional electronic distribution, and a higher density of active sites can be incorporated through synergistic effects effective toward the OER electrocatalytic phenomenon compared to that single dopant [200]. The development of such dual-heteroatom doped carbon nanomaterials along with transition metals presents a new class of materials, especially to reduce the present issues related to OER application.

Metal-organic framework (MOF) presents a new entity class for developing an active electrode material for OER due to its structural miscellany, high surface area, and different surface morphologies [201]. At the same time, they can also be used as starting materials to produce porous carbon, heteroatom doped carbon, and metal oxide nanoparticles on carbon templates for diversified applications [202, 203]. Numerous reports are available based on the fabrication of N-doped or metal co-doped carbon materials from various MOFs used for HER, ORR, OER, supercapacitors, and sensors [204-209]. However, very few reports are available using dual heteroatom-containing MOFs as heteroatoms-rich ligands are less available. Given the above contexts, rationally designing materials with a high density of active sites is desirable to increase their catalytic activity for practical applications. Dithiooxamide (DTO), mostly studied for the

development of inorganic complexes [210] and ion-selective electrodes [211], could have the potential to solve our quest for a suitable framework. The uniqueness of DTO is ascribed to the existence of both C-N and C-S bonds, which can facilitate the synthesis of carbon matrix with simultaneous incorporation of both S and N-atoms internally. Further, this DTO ligand and suitable transition metals (Zn in our case) can be used to develop frameworks of desired morphology.

Next, materials with well-connected Meso- and micro-pores have been proven to be excellent candidates for enhanced electrochemical performances, resulting from high surface area and hierarchical distribution of charges [212]. Moreover, MOFs with secondary components have been proposed to enhance further the electrocatalytic activity of dual-heteroatom-doped carbon matrix [202, 213]. In this context, a small proportion of Co_3O_4 having enriched oxygen vacancy, and as higher oxidation of Co can be easily stabilized by the presence of additional metal ions, it is expected to help improve the OER performances [214-216]. In the present work, we have synthesized a spherical ZnDTO MOF from DTO (as a source for dual doped N, S carbon) and then active co-doped carbon materials (N/S/Zn doped porous carbon, NSC) were synthesized by the carbonization process. After that, active materials were treated with acid to study further the contribution of transition metal (Zn) towards electrochemical performances. Then, to enhance the catalytic activity of the optimized active material, an optimal amount of Co_3O_4 is used to form composites and compare with commercially available RuO_2 for OER. All the synthesized materials have been well characterized through multiple tools like XRD, FT-IR, FESEM, XPS, BET, contact angle and ICP-M measurements. Our optimized conditions for nanocomposite synthesis result in an enhanced OER performance due to enriched oxygen vacancies, localization of charges by S and N-atoms, and stabilization of Co^{3+} oxidation state by Zn^{2+} ions. Therefore, various aspects of

improving the performance of the active material have been thoroughly investigated, which as a whole could be beneficial to many doing electrochemical research worldwide.

5.2 Results and discussion

5.2.1 Structural analysis

The structural features of all as-synthesized materials are established and compared with their analogues by FT–IR, XRD, and XPS results, especially for available functional moieties, crystalline domains and bonding states, respectively. The complexation behavior in ZnDTO was analyzed first by FT-IR as shown in [Figure 5.1(a)]. The FT-IR spectrum of DTO ligand shows doublet at 3125 and 3292 cm^{-1} related to the $-NH_2$ stretching vibration (symmetrical and asymmetrical); while in the case of ZnDTO, the stretching vibration at 3229 cm^{-1} is attributed due to Zn-N bond and weak N-H stretching vibration appeared at 3292 cm^{-1}. The stretching vibration at 1192 cm^{-1} in DTO and ZnDTO is attributed due to the C=S bond. Some new peaks appeared in the spectrum of ZnDTO at 936 and 556 cm^{-1} due to Zn-S and S-Zn-S bond, respectively, which confirmed the successful synthesis of ZnDTO by complexation of Zn metal with DTO ligand. Stretching vibration corresponding to the C-N bond in DTO is found at 1584 cm^{-1} and in ZnDTO it is shifted to a lower frequency at 1515 cm^{-1} because of the bonding of Zn with N [85]. Vibration frequency appeared at 1657 cm^{-1} due to the C=O group (of PVP) present in ZnDTO. Except for C-H stretching vibration at 2932 cm^{-1}, almost all common vibrational peaks of ZnDTO are present in NSC-5, NSC-7 and NCS-9 but in the diffused state due to carbonization. This stretching vibration appeared at 2932 cm^{-1} due to the C-H group resulting from carbonization [Figure 5.1(b)]. However, in the case of NSC-7AW, all functional groups are present like NSC-7, indicating that except for morphological changes, carbonization and acid treatment do not affect the functionalities. The FT-IR spectra of Co_3O_4 exhibit characteristics peak at 633 and 570 cm^{-1} due to Co (III)-O and

Co (II)-O bonds, respectively [Figure 5.1(c)]. The stretching frequency observed at 3428 cm^{-1} is ascertained due to the moisture absorbed during measurement [217]. FT-IR spectra of Co_3O_4|NSC-7 and Co_3O_4|NSC-7AW exhibit vibration peaks of all functionalities related to individual components indicating that these groups are not affected by given synthesis conditions.

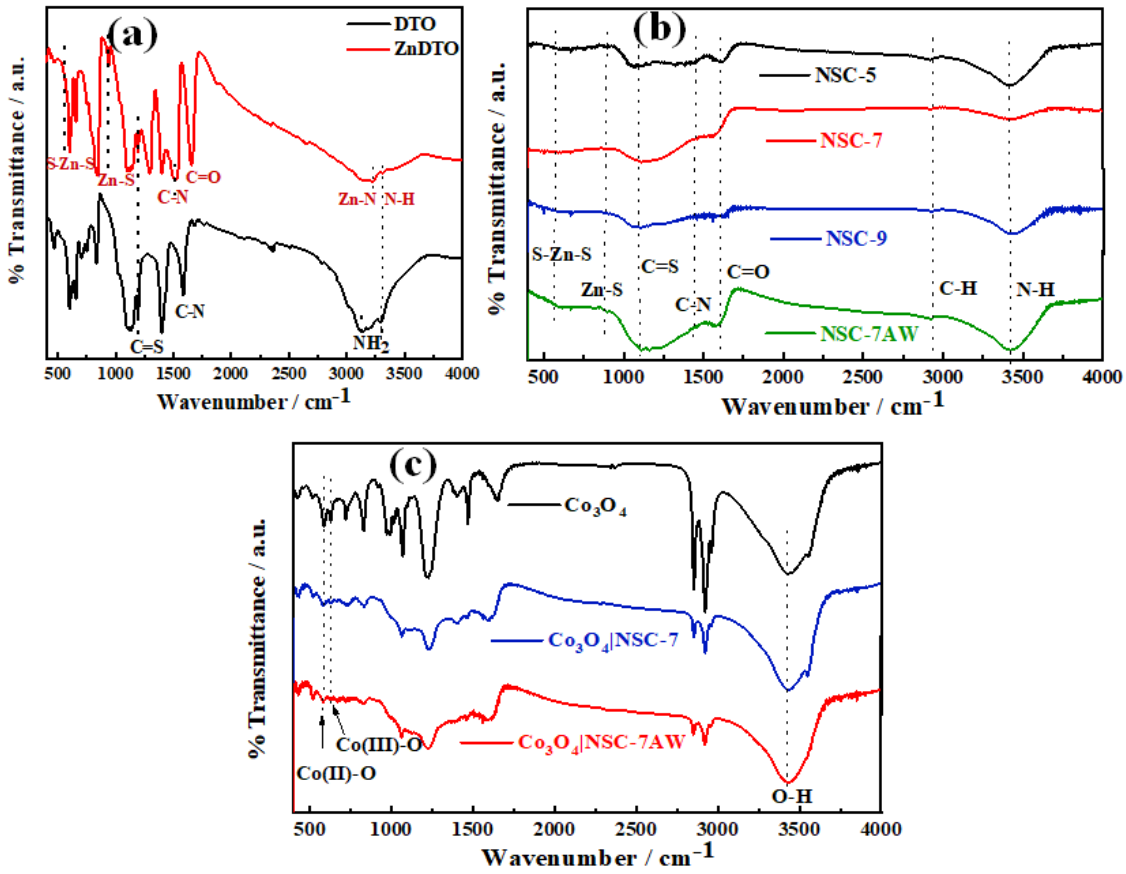

Figure 5.1 FT-IR spectra of (a) DTO, ZnDTO (b) NSC-5, NSC-7, NSC-9, NSC-7AW and (c) Co_3O_4, Co_3O_4|NSC-7 and Co_3O_4|NSC-7AW.

From the crystallinity aspect, ZnDTO reflects similar diffraction peaks as found in the case of CuDTO complex as reported by H. Kitagawa group [85, 218] which supports the successful formation of ZnDTO metal-organic-framework. As shown in [Figure 5.2(a)], ZnDTO exhibits some characteristic polycrystalline diffraction peaks along with some broad amorphous backgrounds. While carbonization of ZnDTO at 700 °C for 3 hours (NSC-7) causes the collapse of spherical morphology into some amorphous aggregates,

which significantly reduces the crystallinity. Further acid treatment of NSC-7 aggregates completely removes their crystalline nature and yields a more amorphous structure, evidenced by its corresponding XRD pattern. After that, Figure 5.2(b) shows the diffraction patterns of Co_3O_4 and it's composite with NSC-7 and NSC-7AW. All the diffraction peaks corresponding to Co_3O_4 represent the formation of a cubic phase (JCPDS No. 01-074-1656). The diffraction peaks corresponding to Co_3O_4 and NSC-7 can be seen in the case of Co_3O_4|NSC-7 which evidenced the retention of its crystallinity after composite formation. However, in the case of Co_3O_4|NSC-7AW, sharp peaks appeared only due to Co_3O_4, as after acid exposure, the crystallinity due to Zn has diminished and its nature was almost as similar to NSC-7AW.

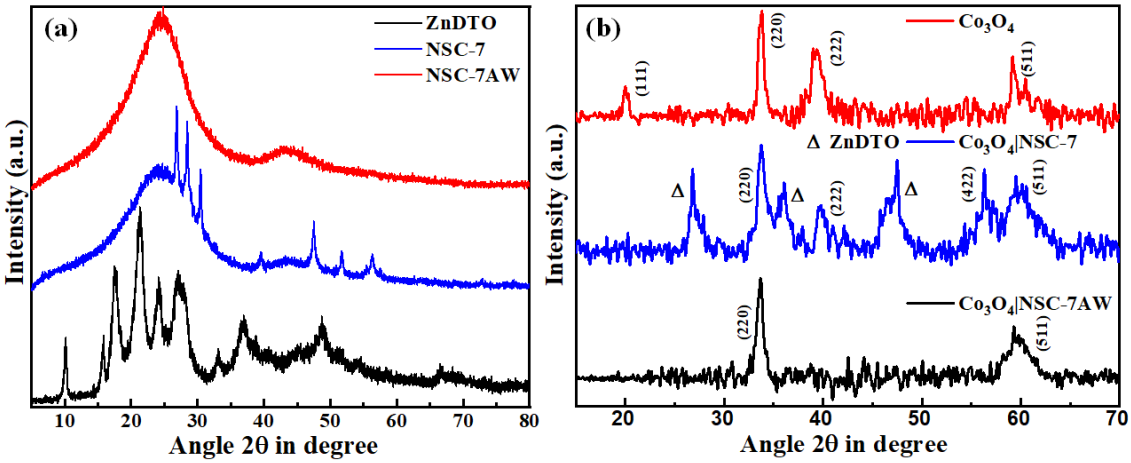

Figure 5.2 Powder XRD of (a) ZnDTO, NSC-7 and NSC-7AW, (b) Co_3O_4, Co_3O_4|NSC-7 and Co_3O_4|NSC-7AW, respectively.

The chemical environment of all possible elements in ZnDTO was analyzed by high-resolution XPS spectrum as shown in [Figure 5.3(a-f)]. Survey spectrum of the ZnDTO framework exhibits C, N, S, O and Zn elements in the material. Herein C, N, S, and Zn are expected from ZnDTO, while the presence of O is observed from PVP. For chemical analysis, individual peaks are deconvoluted and explained one by one. The spectrum of Zn_{2p} displays two peaks at 1021.4 and 1044.4 eV which correspond to $2p_{3/2}$ and $2p_{1/2}$, respectively and confirms the coordination of Zn with DTO ligand when correlated with

the results of other entities [85]. For example, the spectrum of N_{1s} peaks at 397.7, 398.3 and 399.3 eV are attributed to the presence of Zn-N, NH_2 and C-N bonds, respectively [85, 219]. S_{2p} spectrum exhibited two peaks at 161.8 ($2p_{1/2}$) and 163 ($2p_{3/2}$) eV for C-S bond [85]. In the spectrum of C_{1s}, binding energies were observed at 284.6 and 285.9 eV due to C−C and C−N/C−S, respectively. A peak at higher binding energy 287.4 eV also appeared due to C=O (PVP). The XPS spectrum of O_{1s} is deconvoluted into three peaks at 530.5, 531.2 and 532 eV, corresponding to Zn-O, C=O and C-OH groups, respectively [85, 219].

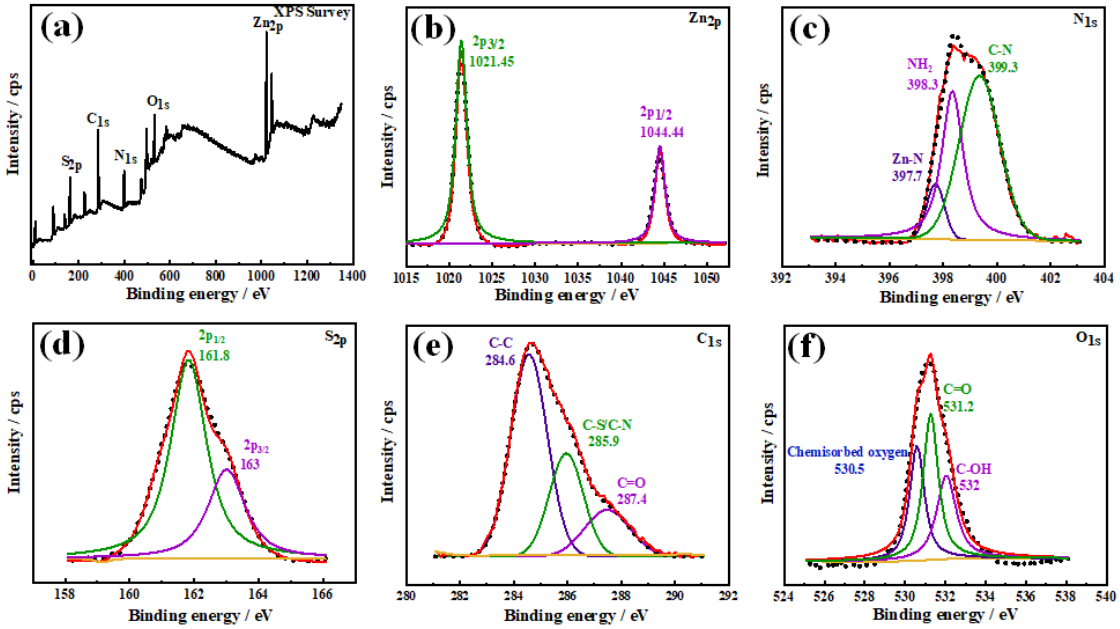

Figure 5.3 XPS for ZnDTO corresponding to (a) XPS survey, (b) Zn_{2p}, (c) N_{1s}, (d) S_{2p} (e) C_{1s} and (f) O_{1s}.

The complete survey of NSC-7 shows the presence of all elements, as seen in the case of ZnDTO [Figure 5.4(a)]. Zn_{2p} shows similar peaks around 1022.18 and 1045.24 eV due to $Zn2p_{3/2}$ and $Zn2p_{1/2}$, respectively. While the amino type of nitrogen in the spectrum of N_{1s} is converted into pyridinic (398.2 eV), pyrrolic (399.6 eV) and graphitic N (400.7 eV) due to carbonization [85]. Spectrum of S_{2p} shows peaks at 162, 163.7 and 165 eV due to Zn-S, C-S-C ($S2p_{3/2}$) and C=S ($S2p_{1/2}$) groups, respectively showing the bonding of S atoms in the carbon structure [85]. Apart from this, some additional peaks also appeared

at higher binding energies (168.3 and 169.9 eV) corresponding to SOx-C group. In the C_{1s} spectrum, peaks are observed at 284.1 eV (C-C sp^2), 284.6 eV (C-C sp^3), 285.2 eV (C-S/C-N), 286 eV (C-O) and 288.3 eV (C=O/C=N) confirm the successful dual doping of heteroatoms (N, S) during carbonization [219]. The presence of a trace amount of oxygen in the full survey spectrum is likely due to the surface moisture. Comparing the XPS of NSC-7AW (Figure 5.5) with NSC-7, it exhibits almost similar results exemplifying the retention of all functional environments.

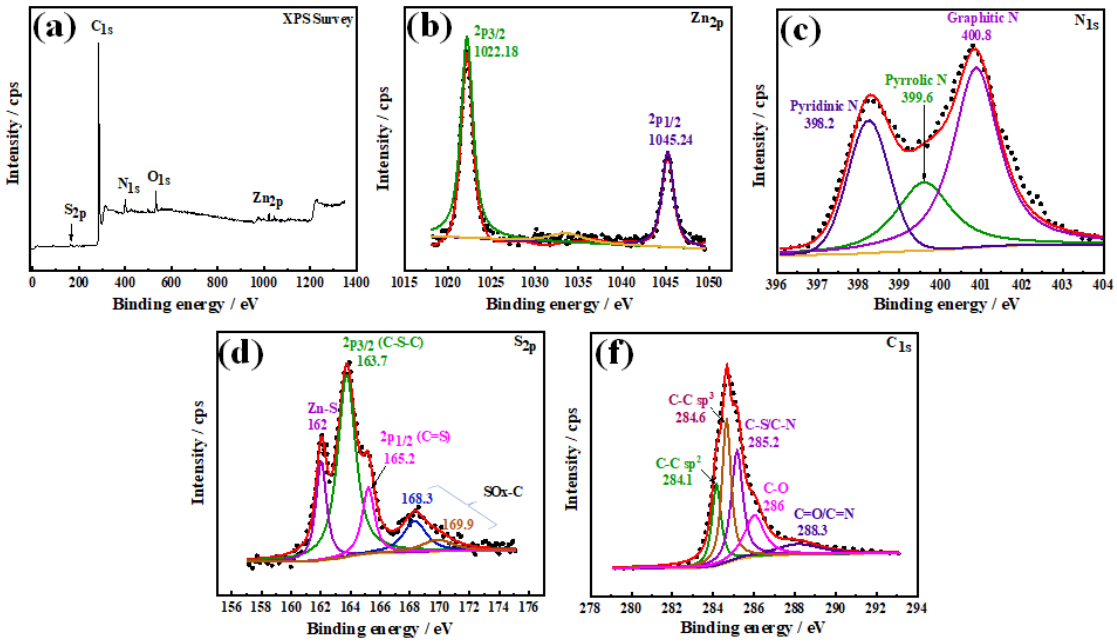

Figure 5.4 XPS of NSC-7 corresponding to (a) survey spectrum, (b) Zn_{2p}, (c) N_{1s}, (d) S_{2p} and (e) C_{1s}.

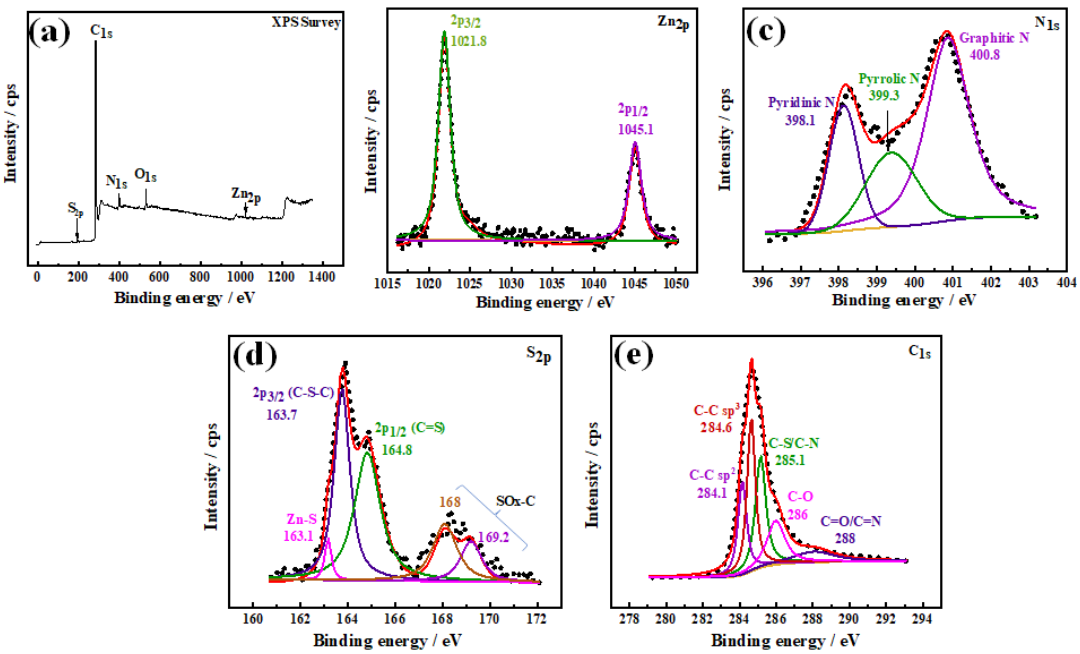

Figure 5.5 XPS of NSC-7AW corresponding to (a) XPS survey (b) Zn_{2p}, (c) N_{1s}, (d) S_{2p} and (e) C_{1s}.

XPS of Co_3O_4 depicts the spectrum corresponding to the various chemical environment of Co_{2p} and O_{1s} (Figure 5.6). The spectrum of Co_{2p} displayed two peaks for Co $2p_{3/2}$ at 782.1 eV and Co $2p_{1/2}$ at 799.2 eV. More precisely, these two peaks can be deconvoluted into four different peaks corresponding to Co^{3+} and Co^{2+} states. Binding energies obtained at 781.8 and 798.1 eV are attributed due to Co^{3+} state. Similarly, peaks found at 783.4 and 799.7 eV are observed due Co^{2+} state. Moreover, two satellite (shake-up) peaks at higher binding energy 786.5 and 803.1 eV were also observed, corresponding to $Co_{2p3/2}$ and $Co_{2p1/2}$, respectively. Based on these results, it is clear that the oxidation state of Cobalt in Co_3O_4 exists as a mixed form of Co^{2+} and Co^{3+}, which can provide enough oxygen vacancies and hence active sites to improve the catalytic activity of nanocomposites [215]. In the case of O_{1s}, three peaks appeared at 531.7, 532.3 and 533.1 eV corresponding to metal-oxygen bonding in Co_3O_4, chemisorbed oxygen and C-OH group respectively [220].

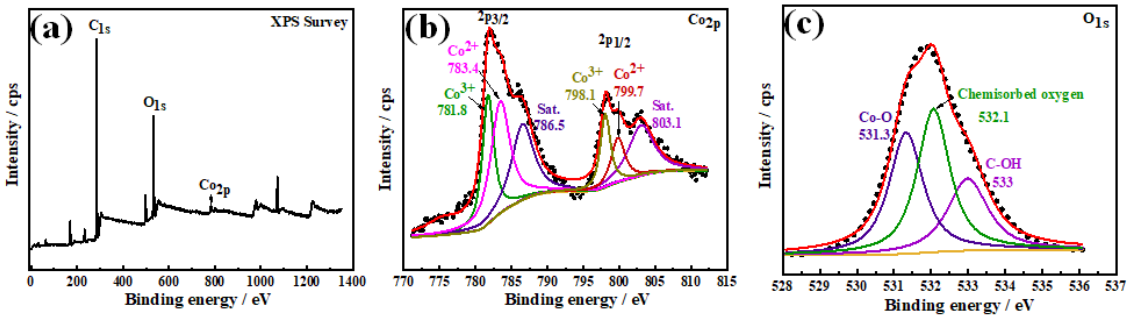

Figure 5.6 XPS spectrum of Co_3O_4 corresponding to (a) survey spectrum, (b) Co_{2p} and (c) O_{1s}.

On the basis of XPS, the bonding states of all possible elements in Co_3O_4|NSC-7 were analyzed and compared with Co_3O_4|NSC-7AW (*cf.* Figure 5.7 and Figure 5.8). In Co_3O_4|NSC-7, the binding energies of all concerned elements are similar to Co_3O_4 and NSC-7. Except for the variation in atomic % of Zn content, all XPS observations of Co_3O_4|NSC-7AW are almost similar to that of Co_3O_4|NSC-7 indicating that exposure of acid is not affecting the bonding environments of all elements (*cf.* Figure 5.8).

A variation in atomic % of Zn, N and S elements of ZnDTO, NSC-7, NSC-7AW, Co_3O_4|NSC-7 and Co_3O_4|NSC-7AW obtained from XPS are tabulated in Table 5.1. This table shows that ZnDTO has the highest contents of these three elements among other materials. However, during the carbonization process followed by the washing steps, a marginal loss of these elements occurs. A loss of Zn is observed in NSC-7AW and Co_3O_4|NSC-7AW catalysts compared to NSC-7 and Co_3O_4|NSC-7, respectively while N and S contents were retained. A slight variation in elemental contents is expected due to the inhomogeneous distribution of elements in the carbon matrix or area-wise variable penetration depths. That is why, a variation in OER properties is observed under similar experimental conditions (as discussed in the electrochemical analysis section). Apart from this, oxygen vacancy also plays an important role in OER performance, as studied by Liu. et. al. [135]. It can be examined through the percentage area of the chemisorbed

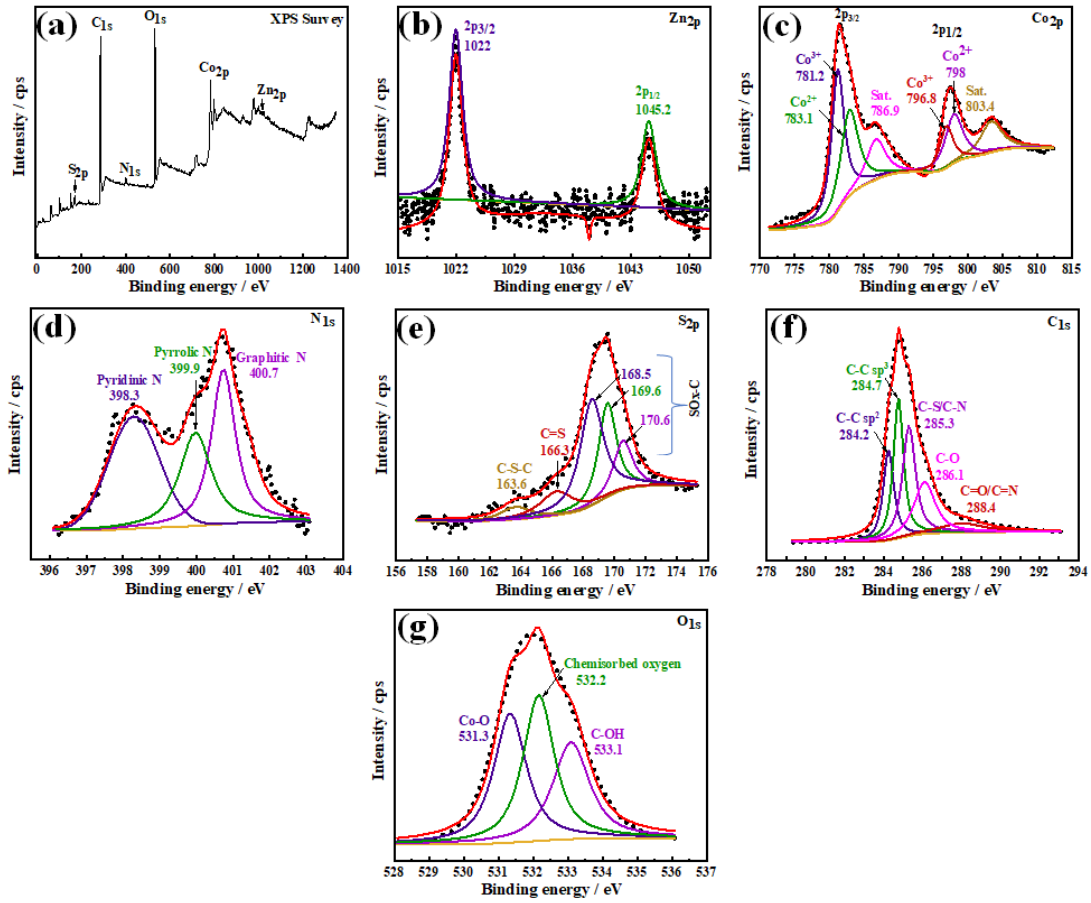

Figure 5.7 XPS of Co_3O_4|NSC-7 corresponding to (a) survey spectrum, (b) Zn_{2p}, (c) Co_{2p}, (d) N_{1s}, (e) S_{2p} and (f) C_{1s} and (g) O_{1s}.

oxygen peak in O_{1s} XPS spectrum of Co_3O_4, Co_3O_4|NSC-7 and Co_3O_4|NSC-7AW. The percentage area of the chemisorbed peak of O_{1s} is found to 63%, 65% and 63% for Co_3O_4, Co_3O_4|NSC-7 and Co_3O_4|NSC-7AW, respectively. Co_3O_4|NSC-7 has more percentage area of the chemisorbed peak than Co_3O_4 and Co_3O_4|NSC-7AW implies more defects (oxygen vacancy) in the catalyst material. Although Co_3O_4 and Co_3O_4|NSC-7AW have the same value but Co_3O_4|NSC-7AW show higher catalytic performance due to the presence of Zn in comparison to Co_3O_4 which has no Zn content (discussed in the electrochemical analysis section). Therefore, the trend in the electrocatalytic performance could be justified in terms of different densities of oxygen vacancy in the Co_3O_4|NSC-7, Co_3O_4|NSC-7AW and Co_3O_4. Oxygen atomic weight percentage has been estimated from XPS measurements around 26.55, 21.75 and 18.93 for Co_3O_4|NSC-7, Co_3O_4|NSC-7AW

and Co_3O_4, respectively. The oxygen vacancy is responsible for generating excess electrons that help bind the adsorbate to the surface of the catalysts via surface-to-adsorbate interaction [7]. Later, it was established that on comparing their stoichiometric materials, oxygen-deficient materials have more impact on OER overpotential. Thus, the best OER performance of Co_3O_4|NSC-7 can be explained because of the highest density of oxygen vacancy compared to other materials, as shown in Figure 5.13(b).

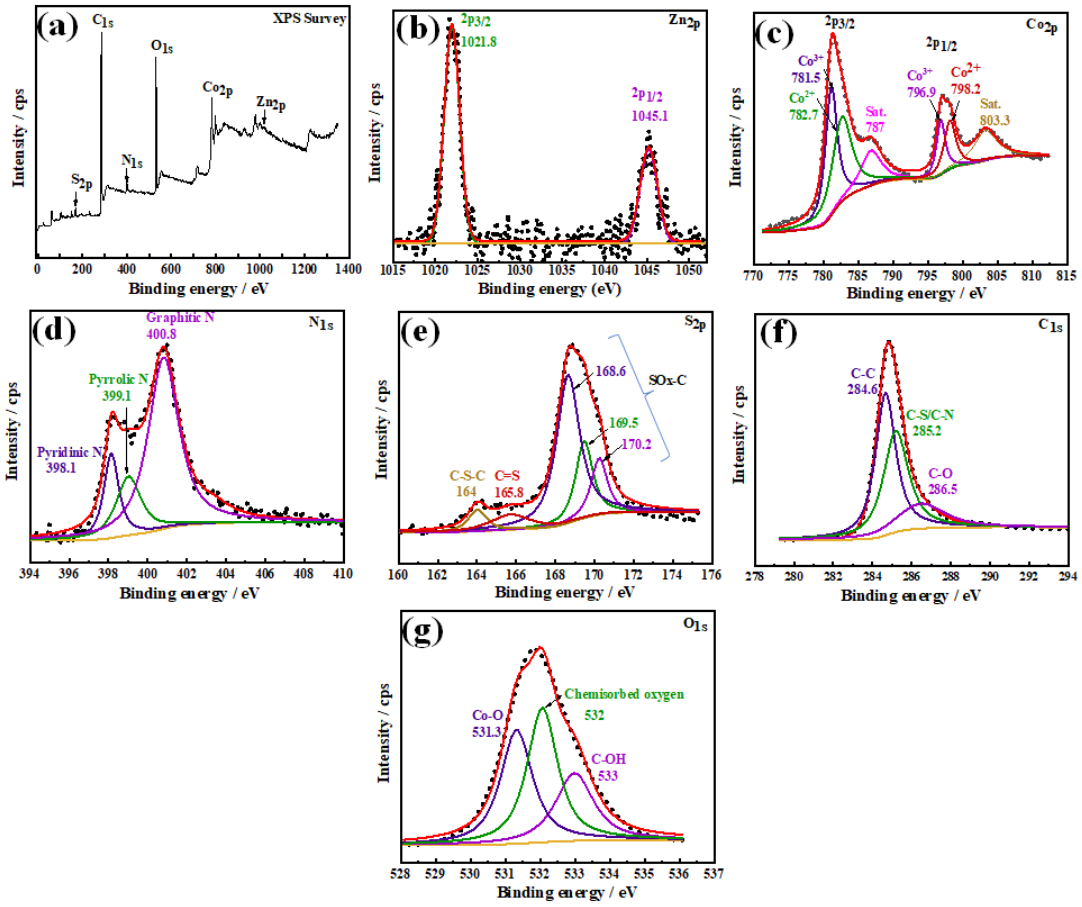

Figure 5.8 XPS of Co_3O_4|NSC- 7AW corresponding to (a) survey spectrum, (b) Zn_{2p}, (c) Co_{2p}, (d) N_{1s}, (e) S_{2p}, (f) C_{1s} and (g) O_{1s}.

Table 5.1 Atomic percentage of Zn, N and, S in catalysts obtained from XPS measurements.

Materials	% Zn	%Co	% N	% S	% O	%C
ZnDTO	6.25	-	13.73	13.2	12.31	54.5
NSC-7	0.45	-	6.54	0.79	5.58	86.63
NSC-7AW	0.2	-	6.72	0.72	4.6	87.76
Co_3O_4|NSC-7	0.36	5.87	6.49	0.71	26.55	66.02
Co_3O_4|NSC-7AW	0.21	4.96	6.75	0.68	21.75	65.65
Co_3O_4	-	2.97	-	-	18.93	78.1

5.2.2 Thermogravimetric Analysis (TGA)

For the selection of carbonization temperatures, a TGA study of ZnDTO was carried out and compared with DTO and PVP (Figure 5.9). This figure shows distinct stages of weight losses for materials with increasing temperature. DTO ligand began to decompose at ~ 140 °C and lost 80.4% of its weight by 246 °C. Next, at 650 °C, it lost most of its contents and was destroyed completely. Pure PVP shows an initial weight loss of about 20% in the range of temperature 18 to 80 °C due to loss of moisture and low molecular weight oligomers. Above this temperature, gradual weight loss occurs until 400 °C due to fragmentation of polymer backbones and functional moieties [85]. After that, a sharp

loss is obtained, followed by the formation of carbons having carbonyl moieties. Similarly, ZnDTO MOF shows three distinct weight loss stages. The first weight loss of 11.4 % was observed between 121 °C and 264 °C, and the second and third weight losses of 18.6% and 12.3% were found at 308 °C and 400 °C, respectively, due to the elimination of the carbon-containing gaseous products leaving behind pores in the carbon skeletons [221]. After 500 °C, a meagre amount of weight loss or almost flat regions appeared, so we randomly chose these regions as 500 °C, 700 °C and 900 °C for carbonization purposes.

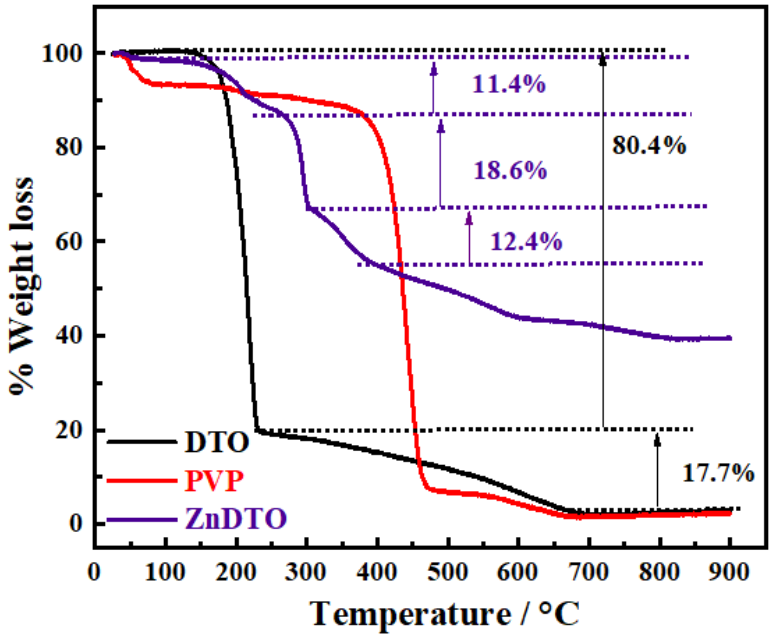

Figure 5.9 TGA of DTO, PVP and ZnDTO.

5.2.3 Morphological analysis

The morphological texture of ZnDTO, NSC-5, NSC-7, NSC-9, NSC-7AW, Co_3O_4, Co_3O_4| NSC-7 and Co_3O_4|NSC-7AW were analyzed by HR-SEM. ZnDTO is composed of well-separated spherical morphology in the order of 1-2 µm in size; some spherical textures are collapsed together and acquire diffused shapes [Figure 5.10(a)]. When subjected to carbonization at 500 °C (NSC-5), the spherical morphology is destroyed and

elongated in an irregular manner. This is due gradual degradation of DTO ligand along with PVP (as seen in TGA curve). Further on increasing the temperature to 700 (NSC-7), the size of particles become smaller leaving behind randomly oriented pores. However, beyond this temperature, i.e., at 900 °C (NSC-9), smaller particles collapse together, and pores are being decreased [*cf.* Figure 5.11(b)]. NSC-7AW is highly porous due to the removal of Zn metals by HCl [Figure 5.10(c)]. As-synthesized Co_3O_4 has a granular-like morphology in the nanometer range due to high surface energy, and it exists in diffused form in its powder state [Figure 5.10(d)]. When it is composited with NSC-7 and NSC-7AW, Co_3O_4 nanoparticles adhere inhomogeneously to these surfaces and retain their morphology [see Figure 5.10(e) and (f)].

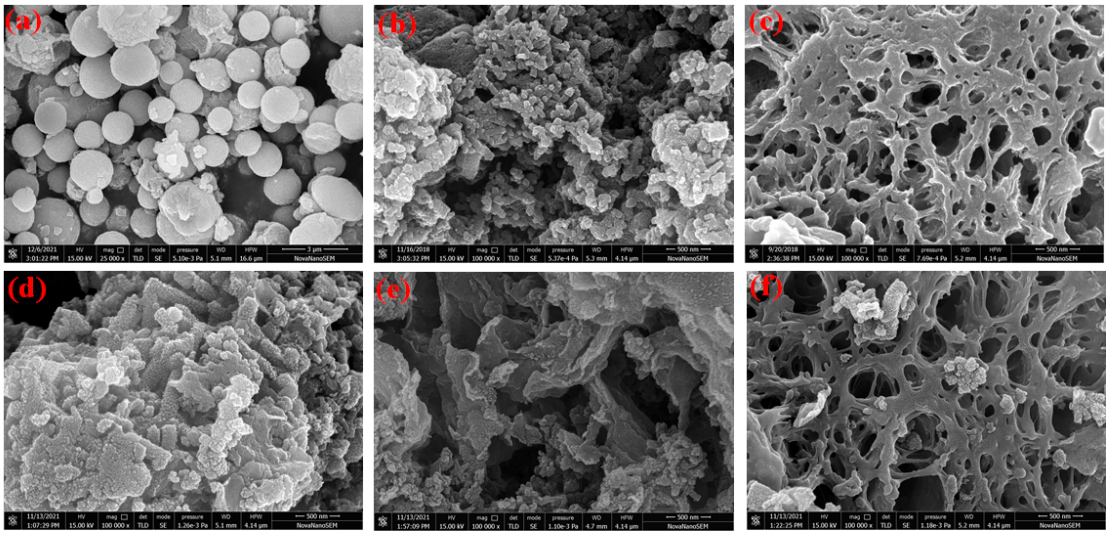

Figure 5.10 FE-SEM images of (a) ZnDTO, (b) NSC-7, (c) NSC-7AW, (d) Co_3O_4, (e) Co_3O_4|NSC-7 and (f) Co_3O_4|NSC-7AW.

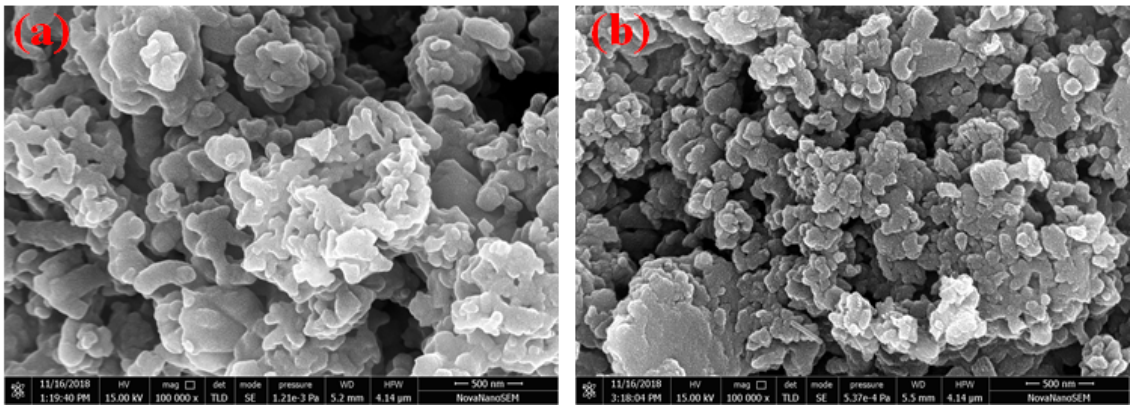

Figure 5.11 FE-SEM images of (a) NSC-5 and (b) NSC-9.

5.2.4 BET measurement

The pore size, surface area, pore volume and pore size distribution of NSC-7, NSC-7AW, Co_3O_4|NSC-7 and Co_3O_4|NSC-7AW catalysts were analyzed with BET and BJH method. Details of BET parameters are presented in Table 5.2. The N_2 adsorption-desorption isotherms and their respective pore size distribution curves (inset) were presented in Figure 5.12. All isotherm plots show mesoporous nature with Type IV isotherm [7, 222]. NSC-7 has the lowest surface area with a larger pore diameter than the NSC-7AW because on acid treatment, porosity increases due to the removal of complexed Zn (in NSC-7) leaving behind the irregular pores. Co_3O_4|NSC-7 shows the largest surface area among all due to exfoliation of NSC-7 during composite formation with Co_3O_4. That is why we are observing higher contact angle as discussed in section 5.2.5. The surface area of Co_3O_4|NSC-7-AW is lower than NSC-7AW and Co_3O_4|NSC-7 due to blocking of pores.

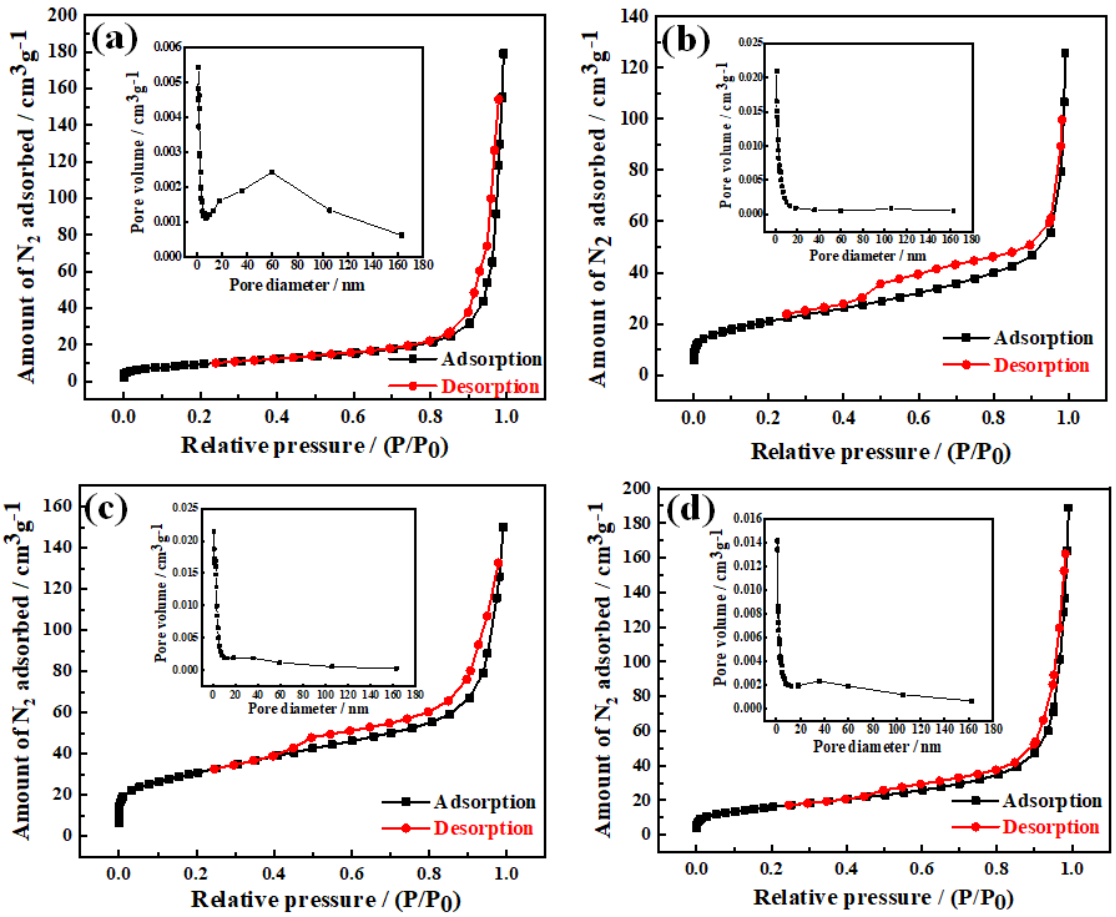

Figure 5.12 N_2 adsorption-desorption isotherms of (a) NSC-7, (b) NSC-7AW, (c) Co_3O_4|NSC-7 and (d) Co_3O_4|NSC-7AW. The corresponding pore size distribution curves are shown in inset.

Table 5.2 BET parameters of the catalysts.

	BET surface area (m^2g^{-1})	**Pore Volume ($cm^3\ g^{-1}$)**	**Pore diameter (nm)**
NSC-7	34.2	0.2638	30.83
NSC-7AW	74.6	0.1862	9.98
Co_3O_4|NSC-7	109	0.2271	8.34
Co_3O_4|NSC-7AW	58.3	0.2845	19.52

5.2.5 Contact angle measurements

In order to understand the role of surface wettability on the electrochemical response, we performed water contact angle measurements on the films prepared on silicone substrates through spin-coating (Table 5.3). For comparison purposes, all measurement conditions were kept the same. Surface wettability and surface energies of these solid surfaces can be correlated through the analytical Young's relation [223] as given below:

$$\cos\theta_w = \frac{\gamma_s - \gamma_{sl}}{\gamma_l} \qquad \text{(Eq. 5.1)}$$

where θ_w, γ_s, γ_l and γ_{sl} represent water contact angle, surface energies (surface tension) of solid-vapor, liquid-vapor and solid-liquid respectively. It is well known that for purely hydrophobic surfaces $\theta_w > 90°$ and for hydrophilic surfaces, $\theta_w < 90°$. As shown in Table 5.3, all the characteristic water contact angles are found to be less than 90° explaining that all the samples allow hydrophilic interaction with the electrolyte while performing the electrochemical measurements. Among all the samples, Co_3O_4 has the lowest contact angle due to the presence of hydroxylated O-H groups. The contact angle of NSC-7AW increased from 43.9 to 58.53° after acid treatment of NSC-7. This is due to the increased surface area that results number of dangling bonds on facets of NSC-7AW which are normally assumed to be hydrophobic in nature. However, in case of Co_3O_4|NSC-7 and Co_3O_4|NSC-7AW, the overall contact angles should be less than NSC-7 or NSC-7AW, as Co_3O_4 surfaces are more hydrophilic. But, the contact angle is observed higher due to the exfoliation of NSCs component during processing. In spite of these, momentarily the improved electrochemical performances were observed due to the dominancy of Co_3O_4 component.

Table 5.3 Contact angle of the catalysts.

Catalysts	Contact angles	
NSC-7	43.90±1.08	
NSC-7AW	58.53±0.88	
Co_3O_4	16.08±0.50	
Co_3O_4|NSC-7	56.43±0.93	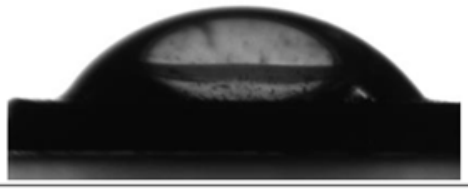
Co_3O_4|NSC-7AW	59.77±2.31	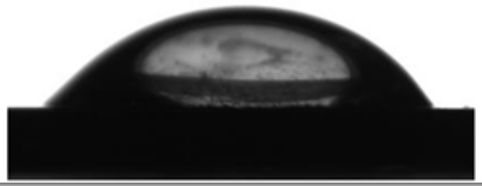

5.2.6 Inductively coupled plasma mass spectrometry (ICP-MS)

The content of the Co and Zn elements in Co_3O_4|NSC-7 and Co_3O_4|NSC-7AW was analysed with Agilent 7800 ICP-MS, US. Prior to measurement, a dispersion of 15 gmL^{-1} of both samples were digested using the following steps [224]. First of all, 150 mg of either material was taken in a Teflon container containing 1 mL HCl (11.6 M) and 3 mL HNO_3 (16 M). After that, this mixture was kept in an autoclave at 200 ℃ for 30 minutes. 6 mL DI water (deionised water) was also added into the above solution after cooling down to room temperature. Finally, as-digested solution was filtered with 0.2 µm

PTFE filter paper. The concentration and percentage of Co and Zn in Co_3O_4|NSC-7 and Co_3O_4|NSC-7AW samples are given in the Table 5.4 below:

Table 5.4 Amount of Co and Zn in Co_3O_4|NSC-7 and Co_3O_4|NSC-7AW.

Material	**Dispersion (mgL^{-1})**	**Co (mgL^{-1})**	**Zn (mgL^{-1})**	**% Co**	**% Zn**
Co_3O_4|NSC-7	15000	5.0	0.81	0.033	0.0054
Co_3O_4|NSC-7AW	15000	4.86	0.03	0.032	0.0002

5.2.7 Electrochemical analysis

5.2.7.1. OER study

The OER performance of all as-synthesized catalysts was studied and compared by LSV, EIS and Tafel slope. First of all, ZnDTO, NSC-5, NSC-7 and NSC-9 were selected and compared to each other to find the best candidate for OER application. As depicted in Figure 5.13(a), with increasing the carbonization temperature from 500 to 700 °C, the OER current first increases, and then gets reduced on further increasing the temperature to 900 °C. The increment in current is expected due to the opening of pores in the NSC-7, while the loss in catalytic activity is because of disruption of the structural morphology, which are visible in SEM images [*cf.* Figure 5.11(b)]. Tafel slope is expected to be an inherent property of the catalyst and another way to understand the catalytic performance. Tafel slopes for ZnDTO, NSC-5, NSC-7, NSC-9 and NSC-7AW (discussed after NSC-7) are calculated for the entire overpotential range because in these catalysts current density does not reach 10 mA cm^{-2}. These Tafel slopes are well fitted by the analytical Tafel Equation (Eq. 1.40). The values are found 218, 203, 135 and 157 $mVdec^{-1}$ for ZnDTO, NSC-5, NSC-7 and NSC-9, respectively. It has been observed that NSC-7 possesses the lowest value (135 $mVdec^{-1}$) among the others [*cf.* Figure 5.13(a')]. It means

NSC-7 has better catalytic activity towards OER than ZnDTO, NSC-5 and NSC-9. Further, the charge transfer kinetics of adsorbed intermediates at the electrode interface was investigated and compared by EIS in the form of Nyquist plot [Figure 5.14(a)]. In general, the formation of the semicircle at Z_{real}-axis is the direct consequence of resistance to charge transfer (R_{ct}), including solution resistance if curvature initiates from origin [106]. If solution resistance is considered almost the same in either case of EIS measurement, it is evident that NSC-7 has the smallest curvature of semicircle compared to NSC-5, NSC-9 and ZnDTO. It means that NSC-7 exhibits the lowest charge transfer-resistant during OER due to optimal pores favourable for the highest charge accumulation near the electrode surface. Thus, up to this end, NSC-7 is optimized and considered the best catalytic material compared to NSC-5, NSC-9 and ZnDTO. After that, only NSC-7 is used to extend the next experiments. Since we observed the presence of Zn during XPS, NSC-7 is treated with 2M HCl (designated as NSC-7AW) and further checked for OER performance to know the contribution of Zn. At the same time, a nanocomposite is created using nano Co_3O_4 in order to cross the limiting barriers of NSC-7. LSV, Tafel slope calculation and EIS were done to compare OER activity [Figure 5.13(b-b') and 5.14(b)]. From Figure 5.13(b), it is exemplified that the NSC-7AW possesses a slightly higher OER current response (lower Tafel slope value of 114 $mVdec^{-1}$) than that of NSC-7 due to the removal of Zn-metals leaving behind pores as seen in SEM [Figure 5.10(c)]. Co_3O_4 nanoparticles exhibits much enhanced OER performance compared to that of NSC-7 or NSC-7AW due to the dominancy of Co^{3+} ions in the stabilization of oxygen vacancies in nanoparticles for the OER [129]. However, both Co_3O_4|NSC-7 and Co_3O_4|NSC-7AW exhibit higher current response than Co_3O_4 nanoparticles or even state of the art catalyst RuO_2, due to the inclusion of porosity from N/S/Zn-doped carbon matrixes along with simultaneous stabilization of Co^{3+} oxidation state by Zn [225]. On comparing the

Co_3O_4|NSC-7 and Co_3O_4|NSC-7AW, Co_3O_4|NSC-7 possess better activity than Co_3O_4|NSC-7AW due to the dominancy of relatively higher concentration of Zn, which causes more contribution towards stabilization of higher oxidation of Co-metal over the contribution of pores present in the matrix. Also the ICP-MS supports this evidence as Co_3O_4|NSC-7AW has low amount of Zn (as given in Table 5.4). Hence, it is concluded that the contribution of both Zn and Co (as in the case of Co_3O_4|NSC-7) is important to enhance the OER performance as per the mechanism discussed later. On comparing the OER performance of Co_3O_4|NSC-7 with state of art catalyst RuO_2, Co_3O_4|NSC-7 exhibit enhanced properties at comparable onset potentials and overpotentials (Co_3O_4|NSC-$7_{(onset\ potential)}$ = 1.71 V *vs.* $RuO_{2\ (onset\ potential)}$ = 1.69 V; Co_3O_4|NSC-$7_{(overpotential)}$ = 480 mV vs. $RuO_{2\ (overpotential)}$ = 460 mV with respect to RHE). Further, to understand the reaction mechanism of the catalysts, the Tafel slope is a very good tool. For a good electrocatalyst, the Tafel slope value should be low. Tafel slopes of Co_3O_4, Co_3O_4|NSC-7, Co_3O_4|NSC-7AW and RuO_2 are calculated up to the overpotential of 10 mA cm^{-2}. Co_3O_4|NSC-7 shows the lowest Tafel slope of 72 $mVdec^{-1}$ among the Co_3O_4|NSC-7AW (84 $mVdec^{-1}$), Co_3O_4 (107 $mVdec^{-1}$) and RuO_2 (112 $mVdec^{-1}$). The Tafel slope value of Co_3O_4|NSC-7 is very close to the featured Tafel slope of 60 $mVdec^{-1}$, suggesting that the rate-determining step should be the H_2O removal and O* formation [step 2 of the OER mechanism, section 1.3.1.1(a)] [226]. Whereas in Co_3O_4, Co_3O_4|NSC-7AW and RuO_2 the Tafel slopes values are close to the standard value of 96 mV dec^{-1}, 110 mV dec^{-1} and 122.2 mV dec^{-1}. These values imply that the OER process in Co_3O_4, Co_3O_4|NSC-7AW and RuO_2 is limited at the first stage [step 1 of the OER mechanism, section 1.3.1.1(a)] where the surface of the catalyst was strongly bonded with -OH groups (reaction order = 1 with respect to OH^- species with featured Tafel slope of 120 mV dec^{-1}) [227]. The higher current density and

lower Tafel slope of Co_3O_4|NSC-7 also justifies from the Nyquist plot (discussed later) which shows that it has the lowest R_{ct} than other counterparts [Figure 5.14(b)].

The synergistic effect between the NSC-7 and Co_3O_4 in Co_3O_4|NSC-7 and Co_3O_4|NSC-7AW are examined through the current density at different mass loading of the catalysts and by quantifying the electrochemically active surface area (ECSA). Firstly, current densities are compared by loading of 0.071, 0.14 and 0.21 mg cm^{-2} of each catalysts through LSV at a scan rate of 5 mVs^{-1}. Maximum current density (j) developed by the catalysts at these mass loadings are presented in [Figure 5.13(c)]. From figure, it is visible that as the mass loading increases from 0.071 mg cm^{-2} to 0.14 mg cm^{-2}, the current density increases but, as we further increase the mass loading to 0.21 mg cm^{-2}, the current density decreases. The reason is that a very low amount of the catalyst (0.071 mg cm^{-2} mass loading) is not sufficient to cover the entire active surface of the electrode (glassy carbon electrode, GCE) by which a minimum electrode-electrolyte interactions occurs and a low current density get. However, as we increase the mass loading to 0.14 mg cm^{-2}, the current density increases because of the more participation of catalyst material in electrode-electrolyte interaction. On further increasing the mass loading from 0.14 to 0.21 mg cm^{-2}, current density get started to decrease because higher mass loading increases the thickness of the catalyst material on the electrode surface which in turn increases the resistivity of the catalyst. This produces a hindrance for the electrolyte from accessing all the electrode surfaces. Thus, 0.14 mg cm^{-2} mass loading is the optimal mass loading of the catalysts and all the measurements are carried out at this mass loading. Secondly, ECSA is estimated by using the equation; $ECSA = \frac{C_{dl}}{C_s} * A$, where, C_{dl} is the double layer capacitance, C_s is the average capacitance of an atomically smooth planar surface of the material per unit area. An average value of C_s, 0.04 mF cm^{-2} is taken [228]. A is the geometric area of the electrode (0.07 cm^2). For C_{dl} calculation CVs of the catalysts are

performed in the non-faradic region from 1.11 to 1.41 V vs. RHE at varying scan rates from 10 to 150 mVs^{-1}. Then the difference between the anodic and cathodic current density ($\Delta j_{1.27} = j_a - j_b$) versus scan rate is plotted as shown in Figure 5.16(a). The C_{dl} value is calculated as half of the linear slope. Co_3O_4|NSC-7 give rise to a higher C_{dl} value (5.92 $mFcm^{-2}$) among the other counterparts inferring the higher ECSA (10.36 cm^2). Figure 5.13(d) shows the plot of ECSA versus the current density of the catalysts in which Co_3O_4|NSC-7 generate maximum current density due to the involvement of a more electrochemically active surface area.

Nyquist plots of NSC-7, NSC-7AW, Co_3O_4, Co_3O_4|NSC-7, Co_3O_4|NSC-7AW and RuO_2 have been compared, and trends are shown in Figure 5.14(b). EIS of NSC-7, measured at applied overpotential (η) of 550 mV, possesses the largest R_{ct} value among other materials. However, this R_{ct} curvature decreases due to the porous nature of NSC-7AW at a similar overpotential. EIS of Co_3O_4, Co_3O_4|NSC-7 and Co_3O_4|NSC-7AW are measured at overpotential (η) of 480 mV; where Co_3O_4, Co_3O_4|NSC-7 and Co_3O_4|NSC-7AW exhibit two quasi-semicircles in both high as well as low-frequency regions. The formation of the semicircle in low-frequency regions is associated owing to the adsorption/desorption of (H^+/OH^-) reactive intermediates by relaxation and diffusion of charge-associated surface intermediates. In contrast, the formation of another semicircle in at higher frequency region is responsible for charge transfer resistance (R_{ct}) [7, 154]. All these Nyquist plots are fitted with Z-Simpin software (EC model). Among the Nyquist plots, the plot of NSC-7 and NSC-7AW is best fitted with RQR ($R_{sol}QR_{ct}$) circuit [*see* Figure 5.15(a)], whereas the Nyquist plots of Co_3O_4, Co_3O_4|NSC-7 and Co_3O_4|NSC-7AW are fitted with the inclusion of capacitive (C) component and corresponding resistances (R).

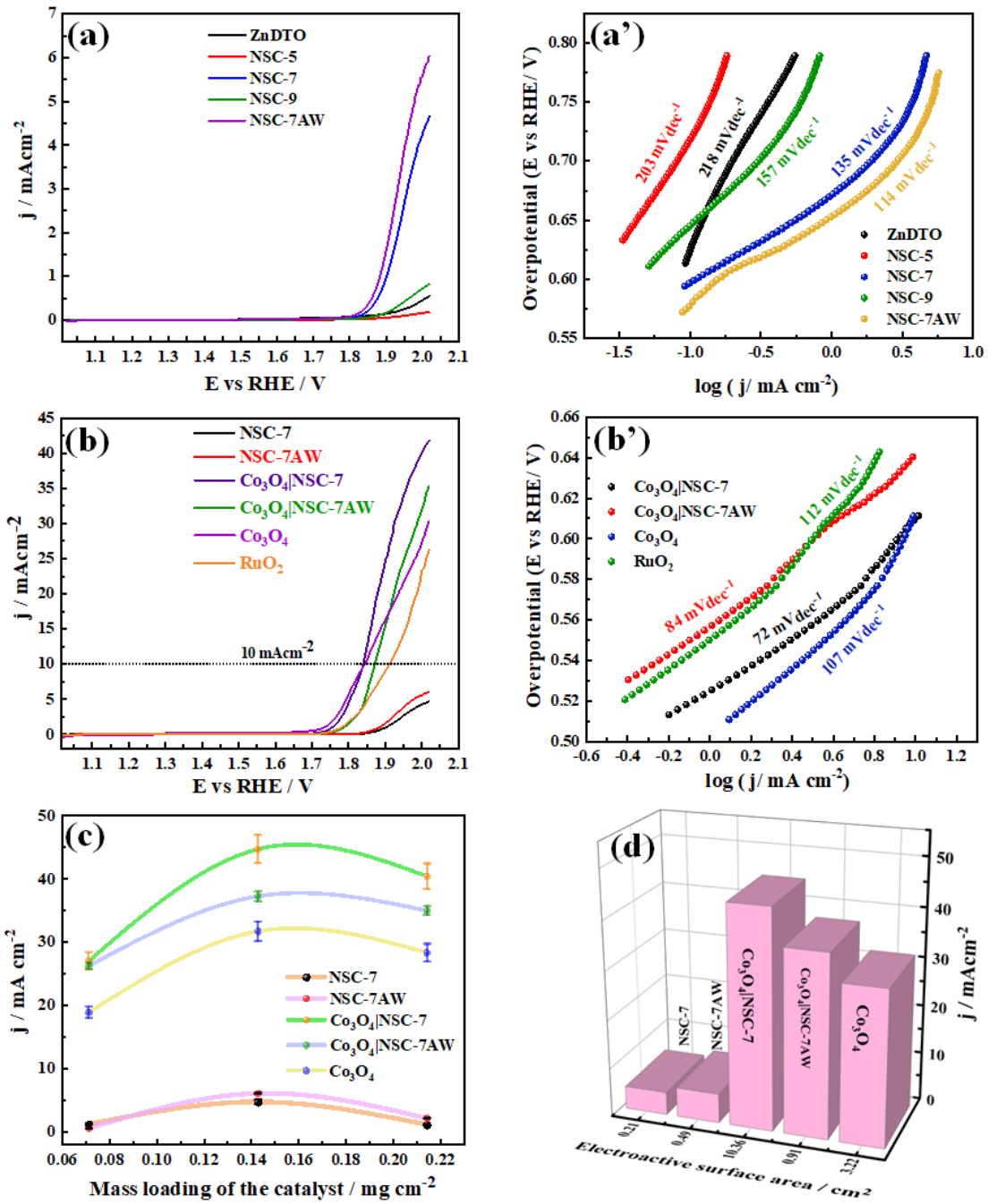

Figure 5.13 Linear sweep voltammograms of ZnDTO, NSC-5, NSC-7 and NSC-9 at scan rates of 5 mVs^{-1} (a') corresponding Tafel slopes, (b) Linear sweep voltammograms of NSC-7, NSC-7AW, Co_3O_4|NSC-7, Co_3O_4|NSC-7AW, Co_3O_4 and RuO_2 at scan rates of 5 mVs^{-1} and (b') corresponding Tafel plots in 0.5 M KOH. Figure (c) and (d) represents the plot of the current density with respect to mass.

Thus, best fitting was observed with R(QR)(QR)(CR) circuit for simplicity presented as $R_1(Q_1R_2)$ (Q_2R_3) (CR_4) [*see* Figure 5.15(b)]. In this EC model, four types of elements are found, *i.e.*, R_1, Q_1R_2, Q_2R_3 and CR_4. The first element is due to solution resistance (R_{so})

at the electrode/electrolyte interface. While both Q_1R_2, Q_2R_3 and CR_4 denote the combination of resistance (R) and constant phase element (Q) and capacitor (C) connected in series due to inhomogeneous charge distribution on the electrode surface. In the EC model, R_2 and R_3 denote the metal oxide (R_o) and charge transfer resistance (R_{ct}), respectively, whereas R_4 represents the capacitive resistance (R_{cap}) in the medium frequency region. The constant phase element, CPE, is associated with inhomogeneous charge distribution during adsorption/desorption of H^+ /OH^- by a diffusion process [7]. All useful parameters for the catalysts are estimated from the best-fitted circuit and tabulated in Table 5.5 and Table 5.6. The elemental circuits of corresponding catalysts have been shown in the inset of Figure 5.15. Among the ZnDTO, NSC-5, NSC-7, and NSC-9 catalysts, NSC-7 has the lowest R_{ct} than that of ZnDTO, NSC-5 and NSC-9 [*cf.* Table 5.5 of and Figure 5.14(a)] and this EIS result is in well supported with OER performance. However, in the case of NSC-7AW, the R_{ct} value decreases dramatically (conductivity increases) due to relatively high porosity [*cf.* Table 5.5 and Figure 5.14(a)]. Similarly, among the curves of Co_3O_4, Co_3O_4|NSC-7 and Co_3O_4|NSC-7AW, Co_3O_4|NSC-7 exhibits the highest conductivity (least R_{ct}) due to the contribution of both Zn and Co towards OER phenomenon (*cf.* Table 5.6). These EIS findings are also in close agreement with LSV studies. Further, to compare the OER performance of Co_3O_4|NSC-7 and Co_3O_4|NSC-7AW with other reported electrode materials, derived from MOF and other additives, a comparison table was constructed (Table 5.7). This table shows that our present work has competent properties compared to earlier work.

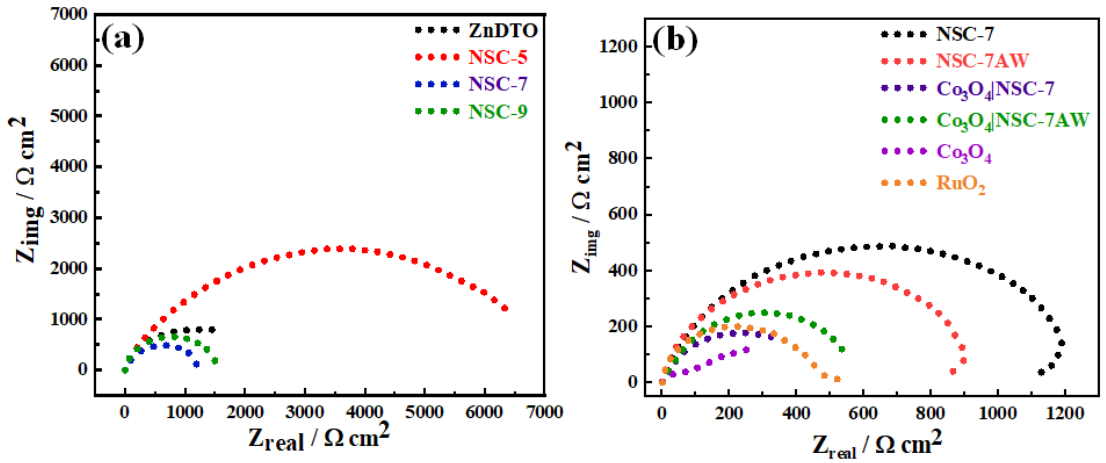

Figure 5.14 Electrochemical impedance spectra of (a) ZnDTO, NSC-5, NSC-7 and NSC-9 and (b) NSC-7, NSC-7AW, Co_3O_4|NSC-7, Co_3O_4|NSC-7AW, Co_3O_4 and RuO_2 in 0.5 M KOH.

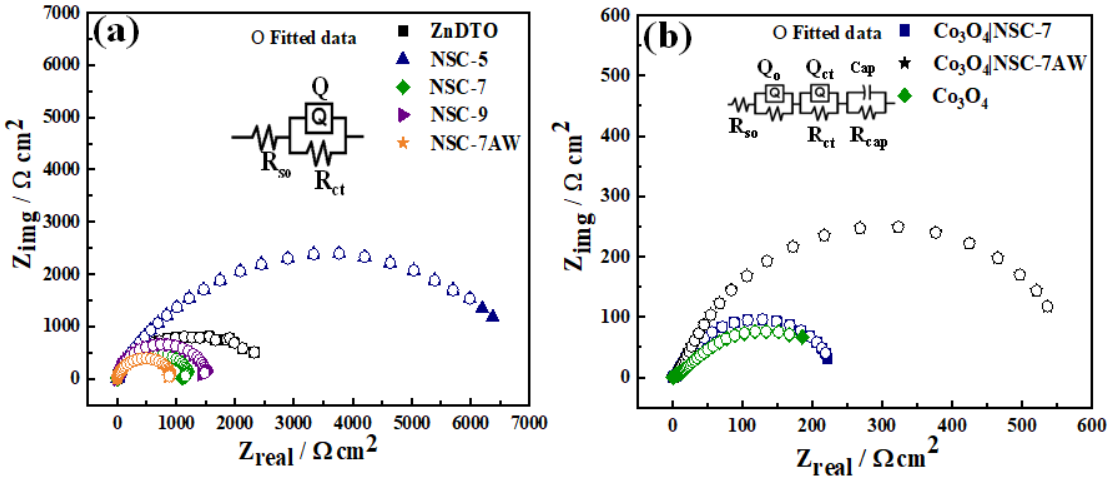

Figure 5.15 EIS fitting of (a) ZnDTO, NSC-5, NSC-7, NSC-9 and NSC-7AW and (b) Co_3O_4, Co_3O_4|NSC-7 and Co_3O_4|NSC-7AW. Inset of each graph shows their representative electrochemical equivalent circuit.

Table 5.5 EIS parameters of the catalysts fitted with R(QR) circuit.

Catalysts	R_{so} (Ωcm^2)	Q ($\Omega^{-1}cm^2S^{\alpha}$)		R_{ct} (Ωcm^2)	Z_{error} (%)
		Y	α		
ZnDTO	1.21	1.60×10^{-7}	0.89	2127	9.32
NSC-5	1.27	2.09×10^{-7}	0.83	6003	11.36
NSC-7	1.16	2.59×10^{-7}	0.84	1235	4.98
NSC-9	1.27	2.38×10^{-7}	0.90	1535	2.49
NSC-7AW	1.23	4.52×10^{-7}	0.87	941	3.43

Table 5.6 EIS parameters of the catalysts fitted with R(QR)(QR)(CR) circuit.

Catalysts	R_{so} (Ωcm^2)	Q_O ($\Omega^{-1}cm^2S^{\alpha}$)		R_O (Ωcm^2)	Q_{ct} ($\Omega^{-1}cm^2S^{\alpha}$)		R_{ct} (Ωcm^2)	C (Fcm^2)	R_{cap} (Ωcm^2)	Z_{error} (%)
		Y_o	α_o		Y_{ct}	α_{ct}				
Co_3O_4|NSC-7	1.45	2.03×10^{-4}	0.65	79.85	1.32×10^{-6}	0.82	3.32	1.55×10^{-5}	150	9.83
Co_3O_4|NSC-7AW	1.49	8.93×10^{-7}	0.89	2.55	1.22×10^{-5}	0.61	172.5	8.70×10^{-6}	413.4	6.52
Co_3O_4	1.24	1.96×10^{-5}	0.64	81.27	2.57×10^{-6}	0.86	7.50	6.30×10^{-5}	118.3	1.57

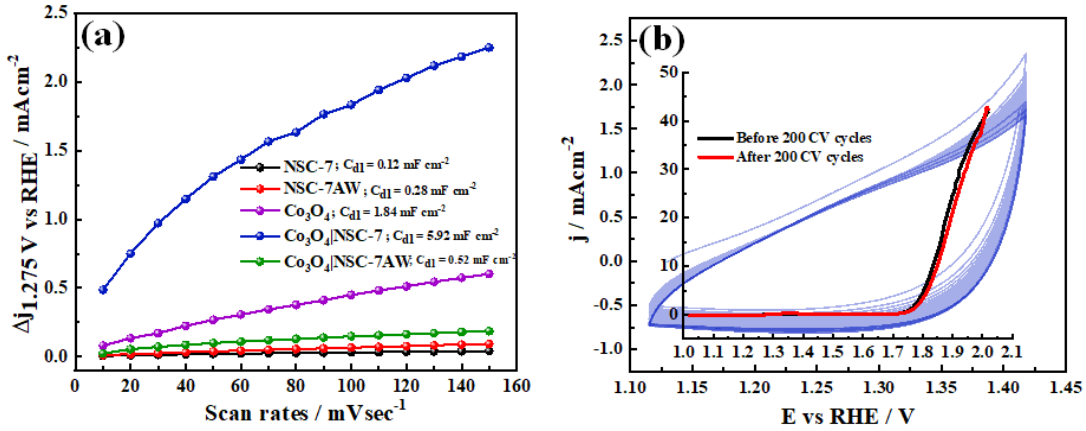

Figure 5.16 (a) Plot of the double layer capacitance (C_{dl}) with respect to scan rates and (b) cyclic stability of Co_3O_4|NSC-7 for 200 CV cycles at 50 mVs^{-1} scan rate. The inset figure shows the LSV curve before and after 200 CV cycles.

5.2.7.2 Mechanism of OER

Generally, there are four electrochemical steps that describe the process of the whole OER process, constituting one proton transfer in an alkaline medium. First of all, at the active sites of metal (M), adsorption and discharge of OH^- occur and the reaction takes place *via* electro-sorption of OH^- ions as given in section [1.3.1.1 (a)]. Thereafter, a number of intermediates such as OH^*, O^*, OOH*, and OO^* are adsorbed on the active sites of metal (M), bounded by M-O followed by the formation of an O-O bond.

In the present case study, the highest electrochemical performance of Co_3O_4|NSC-7 compared to Co_3O_4|NSC-7AW and Co_3O_4 nanoparticle is expected due to the presence of more oxygen vacancies and stabilization of higher oxidation of Co by Zn-metal ions. During OER, Co metal as in octahedral site get oxidized from Co^{3+} to Co^{4+} and lower valence state of Co^{2+} (in tetrahedral site) is stabilized by Co^{3+} [229]. As we know that higher valence state is more conducting than a lower valence state and according to ligand field theory, the electron-donating ability of octahedral sites is stronger than that of tetrahedral sites, indicating that octahedral Co^{3+} is highly benefitted towards O_2^{-2}/ OH^-

displacement during the OER pathway [230]. Co-doped heteroatoms and Zn also enhance the catalytic activity of catalysts. Heteroatoms (N, S) have lone pair of electrons, whereas Zn acts as a strong Lewis acid prone to withdraw electron density from the active sites and contribute to the formation of higher oxidation states of Co (Co^{3+}/ Co^{4+}) and stabilize it, which help in increasing the catalytic activity of the catalyst [231]. At the same time, a higher valence state of Cobalt increases the electrophilicity of surface-oxygen, leading to faster adsorption of OH^- to form the *OOH species, which is regarded as the rate-determining step of OER [232]. Thus, the more atomic percentage of Zn as in the case of Co_3O_4|NSC-7 than Co_3O_4|NSC-7AW (*cf.* Table 5.1) causes more contribution towards the stabilization of a higher oxidation state. That is why Co_3O_4|NSC-7 has better catalytic performance than other counterparts.

5.2.7.3 OER stability test

For any catalyst to be commercialized, its durability and operational stability become essential factors. The current stability at a particular over-potential for an extended period of time is another crucial aspect to justify the performance of an as-developed catalyst. In order to check the current stability of the Co_3O_4|NSC-7 catalyst, the continuous OER was performed by chronoamperometry (CA) process on the application of an overpotential 480 mV *vs.* RHE for two hours (7200 seconds) [Figure 5.17(a)]. It illustrates that a constant current stability 15 $mAcm^{-2}$ for a long duration is achieved, excluding the first 50 seconds. During the early stage of reaction, slight changes in current are expected due to electrolyte diffusion. After 2 hours, an increase in the LSV current is observed, which is approximately 130% times higher than the current observed in the earlier stage of time [Figure 5.17(b)]. This enhancement is expected because of the increment of porosity in the catalyst surface results from the fast diffusivity of ions. This is because a continuous formation of O_2 that leaves the surface for rapid production of more OH^- ions and O_2 (as

shown in the inset of Figure 5.17(a), and it facilitates the ions diffusion [163]. The durability of the Co_3O_4|NSC-7 catalyst is also checked by the continuous 200 CV cycles at 50 mVs^{-1} [Figure 5.16(b)] in the non-faradic region from 1.11 to 1.41 vs. RHE. After the continuous 200 CV cycles, the current density is found almost constant as before CV cycles.

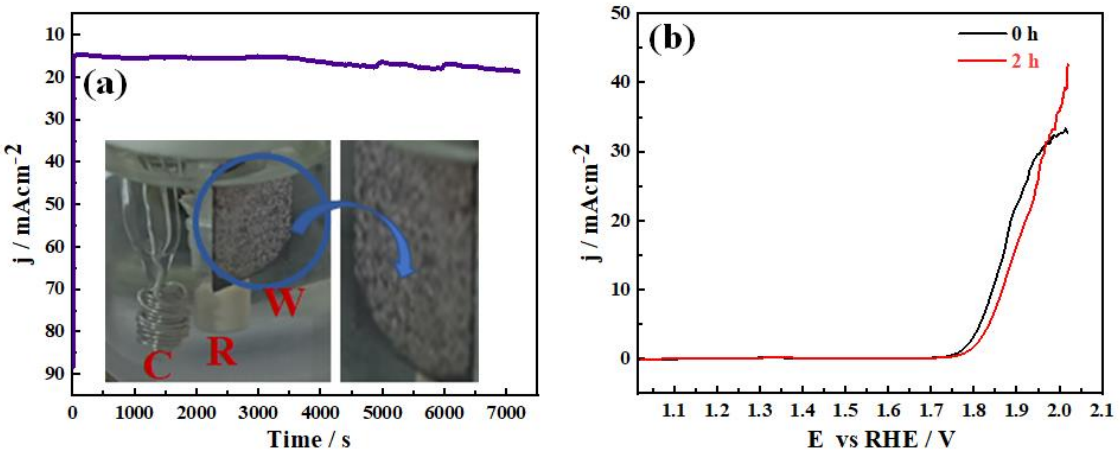

Figure 5.17 (a) Chronoamperometry of Co_3O_4|NSC-7 in 0.5 M KOH for 2 hours and (b) response of LSV current at (I) 0 hour and (II) 2 hours. The inset of figure (a) shows the cell configuration (R-reference, C-counter, W-working electrode). Continuous O_2 bubbles are formed on modified Torey paper during the test.

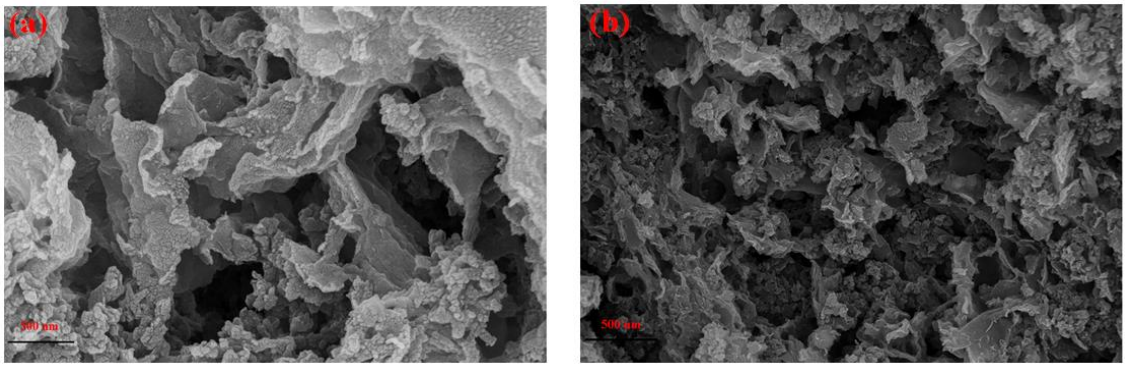

Figure 5.18 FE-SEM images of Co_3O_4NSC-7 (a) before and (b) after chronoamperometry for 7200 seconds in 0.5 M KOH.

Table 5.7 Comparison of OER performance of composite materials derived from MOF and other additives.

S.No.	Electrode materials	Electrolyte	Onset potential (vs. RHE / V)	Potential (vs. RHE / V) at 10 mAcm^{-2}	Tafel slope (mVdec^{-1})	References
1.	(GO 8wt%).Cu MOF	0.5 M H_2SO_4	1.1	-	84	[233]
2.	Co@C-MWCNTs	1 M KOH	1.5	1.6	67	[234]
3.	3DCo@CoNPC-6	0.1 M KOH	1.6	1.7	63	[235]
4.	R@NiFe (1:1)	1M KOH	1.4	1.5	62	[236]
5.	Co_3O_4|NSC-7	0.5 M KOH	1.71	1.83	62	This work
6.	Co_3O_4|NSC-7AW	0.5 M KOH	1.72	1.86	75	This Work

5.3 Conclusions

As-synthesized spherical ZnDTO MOF is being utilized for forming porous NSC-7 at optimized conditions by the carbonization process and tested for OER response. Then, NSC-7 and NSC-7AW have been chosen as active matrices for incorporating a low amount of Co_3O_4 nanoparticles material, resulting in enhanced OER compared to other counterparts and RuO_2. Different characterization tools exemplified that individual component of Co_3O_4|NSC-7 nanocomposite retains their identity after applying consecutive synthesis conditions. Co_3O_4 nanoparticles itself exhibits better OER performance than that of other counterparts (NSC-7, NSC-7AW) due to the involvement

of oxygen vacancies, including the variable oxidation state of Co metal. However, as-synthesized composite, Co_3O_4|NSC-7, exhibits enhanced OER performance than Co_3O_4 nanoparticle due to the Zn and heteroatoms' participation and high oxygen vacancies. It has been found that the acid treatment of NSC-7 causes a loss of Zn percentage that leads to poor performance of Co_3O_4|NSC-7AW in OER. This finding evidenced that contribution of Zn is also much more significant in stabilizing the higher oxidation state of Co, which is responsible for the high conductivity of composites. Co_3O_4|NSC-7 shows the onset overpotential of 480 mV vs. RHE very near the state of art catalyst 'RuO_2' (460 mV vs. RHE) and has the lowest Tafel slope 62 $mVdec^{-1}$. The prepared composite also excels in its current stability test for 7200 seconds at a static overpotential of 480 mV vs. RHE and can exhibit continuous OER performance with a 130 % increment in LSV current as the continuous evolution of oxygen causes increased porosity. This thorough investigation elucidates all different approaches to enhance the catalytic properties of MOF-derived carbon materials, which will help others design suitable active electrode materials for electrochemical applications.